

PAPER

Systematic simulation studies on the penetration of resonant magnetic perturbations in an Experimental Advanced Superconducting Tokamak

To cite this article: H W Zhang *et al* 2021 *Plasma Phys. Control. Fusion* **63** 035011

View the [article online](#) for updates and enhancements.



IOP | ebooks™

Bringing together innovative digital publishing with leading authors from the global scientific community.

Start exploring the collection—download the first chapter of every title for free.

Systematic simulation studies on the penetration of resonant magnetic perturbations in an Experimental Advanced Superconducting Tokamak

H W Zhang^{ID}, X Lin, Z W Ma^{ID}, W Zhang^{ID} and T E Bagwell

Institute for Fusion Theory and Simulation, Department of Physics, Zhejiang University,
Hangzhou 310027, People's Republic of China

E-mail: zwma@zju.edu.cn

Received 31 August 2020, revised 28 November 2020

Accepted for publication 11 December 2020

Published 12 January 2021



Abstract

The penetration properties of the $n = 1$ resonant magnetic perturbations (RMPs) with toroidal rotation are systematically studied by the upgraded three-dimensional toroidal magnetohydrodynamic code CLTx, through both linear and nonlinear simulations. It is found that in the presence of toroidal plasma rotation, the saturation state for high resonant harmonics is obtained in linear simulations due to the mode becoming unlocked from the internal magnetic islands. In nonlinear simulations, nonlinear effects become important when the toroidal plasma rotation is not included. The zonal component resulting from the nonlinear mode coupling is necessary for the saturation of the whole system including the internal kink mode and the $m/n = 2/1$ tearing mode. The simulations of RMP penetration demonstrate that the mode coupling is associated with the toroidal effect rather than nonlinear effects. With a low resistivity $\eta_0 = 10^{-9} \sim 10^{-8}$ close to the experimental value, the single-harmonic-RMP is hard to penetrate the mode-rational surface because of the plasma screening effects, resulting in a truncation of the radial mode structure. On the other hand, the non-resonant components in the multiple-harmonic-RMP could largely reduce the effect of the plasma shielding, which leads to that the RMP is able to penetrate deeply into the central plasma region through the poloidal harmonic coupling.

Keywords: resonant magnetic perturbation, penetration, nonlinear effects, toroidal effect

(Some figures may appear in colour only in the online journal)

1. Introduction

Resonant magnetic perturbation (RMP) is very efficient for controlling the edge localized mode (ELM) [1] in H -mode [2] discharge in tokamaks. Mitigation and/or suppression of type-I ELMs in different tokamaks have been achieved by RMPs, such as the $n = 1$ and 2 RMPs (n represents the toroidal mode number) in an Experimental Advanced Superconducting Tokamak (EAST) [3–5], the $n = 1, 2$ and 4 RMPs in an Axially Symmetric Divertor Experiment (ASDEX) Upgrade [5–8], the $n = 2$ and 3 RMPs in Doublet III device (DIII-D)

[9–14], the $n = 1$ and 2 RMPs in Korea Superconducting Tokamak Advanced Research (KSTAR) [15–17], the $n = 3, 4$ and 6 RMPs in Mega Ampere Spherical Tokamak (MAST) [18–20], the $n = 1$ and 2 RMPs in Joint European Torus (JET) [21], etc. However, magnetohydrodynamic (MHD) theoretical analysis [22, 23], numerical simulations [3, 9–11, 24–33], and plasma experiments [34–36] have demonstrated that RMP penetration theory based on the vacuum model is inaccurate or even completely invalid. Meanwhile, RMP penetration is especially sensitive to plasma response in the presence of dynamical effects, like plasma rotation [29, 32, 37], two-fluid effects

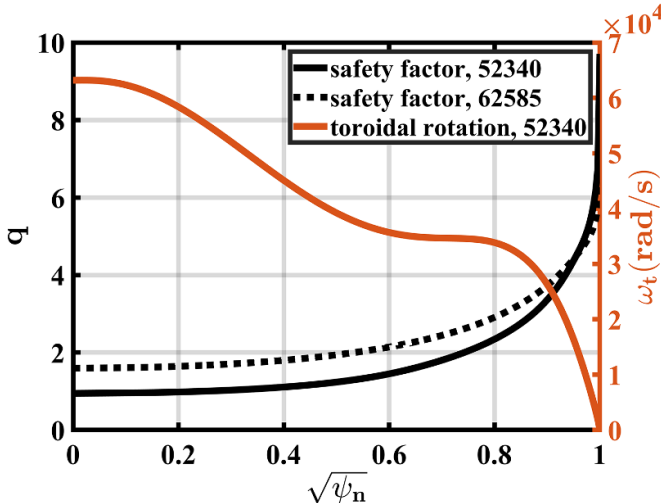


Figure 1. Initial profiles of the safety factor q for EAST discharge 52 340 at 3150 ms and 62 585 at 3800 ms, and the toroidal rotation ω_t for EAST discharge 52 340 at 3150 ms.

[9, 28, 38, 39], screen currents [40, 41], nonlinear mode coupling [25, 28, 32, 42], etc.

Linearized models in analytical and numerical studies of the influence of plasma response on RMP penetration have been widely adopted and have shown high efficiency in calculation speed and great feasibility compared with experimental results. Results obtained by the MARS-F code [43] based on a linearized single-fluid MHD model have successfully explained the offset of the optimal coil phase in ELM control experiments with the $n = 1$ and 2 RMPs in EAST [3, 5] and the $n = 2$ RMP in the ASDEX Upgrade [5, 44]. The simulation results from the M3D-C¹ code [45] adopting a linearized two-fluid model have demonstrated that the penetrated RMP field reaches its maximum value when the perpendicular electron rotation $\omega_{\perp e}$ vanishes at the mode-rational surface [9, 39]. Nevertheless, recent experiments [46–48] and theories [49] find that the RMP penetration is more likely determined by the natural mode frequency with a finite ion diamagnetic drift frequency correction from the $\mathbf{E} \times \mathbf{B}$ velocity, rather than the exact $\omega_{\perp e}$ zero-crossing including the electron diamagnetic drift ω_{se} . In addition, nonlinear simulations of RMPs indicated that nonlinear effects are crucial and exhibit some dynamical features that are not present in purely linear simulations, such as the density pumpout due to the $n = 0$ component coupled with $n = 2$ perturbations [25] and the generation of high-order magnetic islands from the coupling of different harmonics [28]. The resonant amplification of RMPs due to the coupling between the non-resonant kink component ($|m| > |nq|$, where m is the poloidal mode number, and q is the safety factor) and the resonant m component was observed in both linear and nonlinear modeling, respectively, by the MARS-F code [50] and the JOREK code [25]. The validity criterion for the linear model can be written as the overlap condition $|\partial\zeta_r/\partial r| < 1$ (where ζ_r is the plasma displacement normal to the equilibrium magnetic field) after considering plasma response [5, 42]. Although the linear model

has the advantages of being numerically and analytically efficient while still maintaining great validity in RMP calculations, nonlinear mode coupling should not be ignored in some cases [5, 42].

In our previous work [33], the code CLT was upgraded to CLTx for studying RMP penetration in EAST based on the linear and nonlinear resistive MHD equations. Our linear simulation results of the $n = 1$ RMP for the ELM mitigation of discharge 52 340 in EAST agree well with those obtained from the MARS-F code. However, the simulations with different resistivities suggest that the amplitude reduction and the phase shift of the resonant harmonics due to plasma response increase with decreasing the resistivity. In this work, the nonlinear terms are retained in the CLTx code for studying nonlinear effects on RMP penetration. The influences of toroidal rotation, nonlinear mode coupling, and toroidal effect on RMP penetration will be analyzed and discussed. The outline of the present paper is as follows: section 2 introduces the simulation model used in the CLTx code; section 3 presents the results of the linear and nonlinear simulations for RMP penetration and the influences of toroidal rotation; section 4 gives the toroidal effect on RMP penetration in detail; and finally, the results of the present paper are summarized in section 5.

2. Simulation model for CLTx

In the CLTx code, we adopt the full set of single fluid, resistive MHD equations including dissipations [33, 51–53], i.e.

$$\partial_t \rho = -\nabla \cdot (\rho \mathbf{v}) + \nabla \cdot [D \nabla (\rho - \rho_0)], \quad (1)$$

$$\partial_t p = -\mathbf{v} \cdot \nabla p - \Gamma p \nabla \cdot \mathbf{v} + \nabla \cdot [\kappa \nabla (p - p_0)], \quad (2)$$

$$\partial_t \mathbf{v} = -\mathbf{v} \cdot \nabla \mathbf{v} + (\mathbf{J} \times \mathbf{B} - \nabla p)/\rho + \nabla \cdot [\nu \nabla (\mathbf{v} - \mathbf{v}_0)], \quad (3)$$

$$\partial_t \mathbf{B} = -\nabla \times \mathbf{E}, \quad (4)$$

with

$$\mathbf{E} = -\mathbf{v} \times \mathbf{B} + \eta (\mathbf{J} - \mathbf{J}_0), \quad (5)$$

$$\mathbf{J} = \nabla \times \mathbf{B}, \quad (6)$$

where ρ , p , \mathbf{v} , \mathbf{B} , \mathbf{E} , and \mathbf{J} are the plasma density, thermal pressure, plasma velocity, magnetic field, electric field, and current density, respectively. The subscript ‘0’ denotes equilibrium quantities. $\Gamma(=5/3)$ is the ratio of specific heat (also known as the adiabatic index) of the plasma. The variables are normalized as: $\mathbf{B}/B_{00} \rightarrow \mathbf{B}$, $\mathbf{x}/a \rightarrow \mathbf{x}$, $\rho/\rho_{00} \rightarrow \rho$, $\mathbf{v}/v_A \rightarrow \mathbf{v}$, $t/\tau_A \rightarrow t$, $p/(B_{00}^2/\mu_0) \rightarrow p$, $\mathbf{J}/(B_{00}/\mu_0 a) \rightarrow \mathbf{J}$, $\mathbf{E}/(v_A B_{00}) \rightarrow \mathbf{E}$, and $\eta/(\mu_0 a^2/\tau_A) \rightarrow \eta$, where a is equal to 1 m, $v_A = B_{00}/\sqrt{\mu_0 \rho_{00}}$ is the Alfvén speed, and $\tau_A = a/v_A$ is the

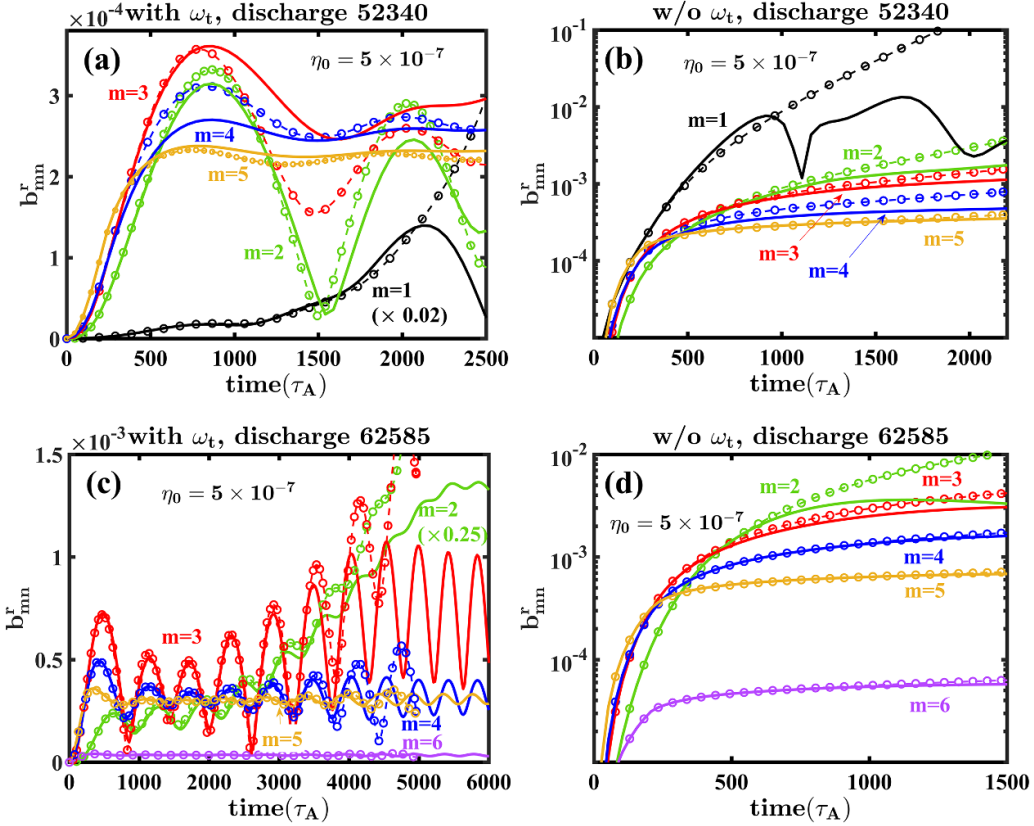


Figure 2. Time evolutions of $n = 1$ resonant harmonics $b_{m/n}^r$ at different rational surfaces with both linear (dashed lines with circles) and nonlinear (solid lines) simulations for discharge 52 340 (in the upper panel) (a) with toroidal rotation (the $m/n = 1/1$ harmonics are artificially reduced by multiplying 0.02 to put them on the same plot with the other harmonics) and (b) without toroidal rotation, as well as for discharge 62 585 (in the lower panel) (c) with toroidal rotation (the $m/n = 2/1$ harmonics are artificially reduced by multiplying 0.25 to put them on the same plot with the other harmonics) and (d) without toroidal rotation. The different line colors correspond to various poloidal harmonics: black ($m = 1$), green ($m = 2$), red ($m = 3$), blue ($m = 4$), yellow ($m = 5$), purple ($m = 6$). Note that the time span in the horizontal axis is very different for each plot. The vertical axis in the left column is scaled linearly, while it is scaled logarithmically in the right column.

Alfvén time. B_{00} and ρ_{00} are the initial magnetic field and plasma density at the magnetic axis, respectively. The Hall term [54] in the generalized Ohm's law is not included. Thus diamagnetic drifts due to two-fluid effects are not present in the current model. The previous studies [9, 28, 37, 39, 42, 55] suggested that the electron diamagnetic drift ω_{*e} could be helpful for RMP penetration due to the reduction of perpendicular electron rotation $\omega_{\perp e}$ at the mode-rational surface in the two-fluid model. However, recent experimental [46–48] and theoretical [49] studies found that the natural mode frequency from the $\mathbf{E} \times \mathbf{B}$ velocity corrected by a small ion diamagnetic drift frequency plays a crucial role in RMP penetration, rather than the exact perpendicular electron rotation $\omega_{\perp e}$.

The simulation domain constructed in the CLTx code has been extended beyond the last closed magnetic surface to the scrape-off layer (SOL) with the inclusion of the X-point. The normalized parameters used in all simulations herein are fixed to be $D = 1 \times 10^{-6}$, $\kappa = 5 \times 10^{-5}$, and $\nu = 1 \times 10^{-6}$. The spatial distribution of the time-independent resistivity is determined by the initial normalized plasma temperature T with $\eta = \eta_0 \times T^{-3/2}$, where η_0 is the resistivity at the magnetic axis and corresponds to a resistivity minimum

since the temperature is maximum at this axis. The normalized resistivity η_0 in usual EAST discharges is of the order of $10^{-9} \sim 10^{-8}$. In the previous simulations of CLTx, the resistivity is chosen to be $\eta_0 = 5 \times 10^{-9}$ that is close to the experimental value of discharge 52 340 [33]. The resistivity used in the present simulations is set to be from $\sim 10^{-8}$ to $\sim 10^{-5}$. The simulations with large resistivities (two or three orders of magnitude larger than the experimental value) are conducted to enhance the physical understanding of RMP penetration, rather than to directly explain the experiments. A mesh consisting of $256 \times 16 \times 256$ points in (R, ϕ, Z) is utilized for all simulations. In the CLTx code, the basic straight field line coordinate $(\sqrt{\psi_n}, \theta_s, \phi)$ [33, 56] is used for spectrum analysis, where $\sqrt{\psi_n}$ is the square root of the normalized poloidal flux ψ_n , θ_s is the generalized poloidal angle, and ϕ is the toroidal angle.

The initial equilibria are reconstructed from EAST discharge 52 340 at 3150 ms [3] and discharge 62 585 at 3800 ms [57] by EFIT (Equilibrium Fitting code) [58]. The safety factor q profiles for each discharge and the toroidal rotation ω_t profile of discharge 52 340 [3] measured by charge exchange recombination spectroscopy [35, 59] are given in figure 1.

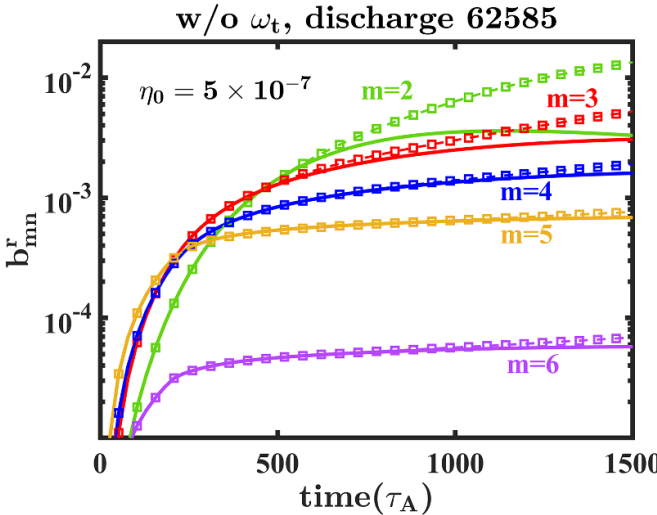


Figure 3. Time evolutions of the $n = 1$ resonant harmonics $b_{m/n}^r$ for discharge 62 585 without toroidal rotation from CLTx nonlinear simulations with (solid lines) and without (dashed lines with squares) the $n = 0$ zonal component.

3. Linear and nonlinear saturations with the presence of RMP

In our previous linear benchmark study for the equilibrium of discharge 52 340, the magnetic island at high rational surfaces ($q > 1$) reaches a saturation stage, however the inner unstable $m/n = 1/1$ kink mode is still in the linear growth stage [33]. To understand the detailed saturation mechanisms of magnetic islands in linear simulations, comparisons between linear and nonlinear simulations with a relatively large resistivity $\eta_0 = 5 \times 10^{-7}$ (about two orders of magnitude larger than the experimental value) are performed in the present section. Such an elevated resistivity can significantly dissipate the screen currents induced by RMPs at the rational surfaces [40, 41], consequently promoting the perturbation penetration dramatically [33]. Although the chosen resistivity is not experimental-related, the increased resistivity can increase the growth rate of tearing mode and reduce the simulation time to reach the final nonlinear saturation stage. In cases with an experimental resistivity, the machine time for nonlinear RMP simulations by CLTx will be enormous. Also, the nonlinear coupling and poloidal harmonic coupling of various harmonics focused on by this work are qualitatively analogous with different values of the resistivity. Consequently, the results obtained with the enlarged resistivity are just qualitatively rather than quantitatively relevant to the experimental results of discharge 52 340 and 62 585. However, they may still help to understand some RMP experimental results generally. In addition, the simulation results with experimental resistivity from CLTx have been reported previously [33]. The RMP coils set up in the CLTx code are $I_{\text{coil}} = 10$ kAt (kilo-Amp-turns), $n = 1$, $\Delta\Phi = 0$, where $\Delta\Phi$ is the relative phase difference between the upper and lower coils [5]. The role of the plasma toroidal rotation on mode saturation is also studied in the present paper by artificially including plasma rotation.

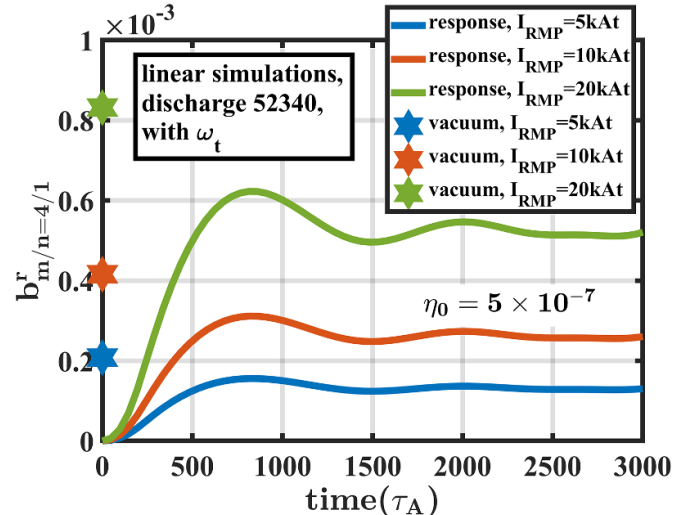


Figure 4. Time evolutions of the resonant harmonic $b_{m/n=4/1}^r$ at the $q = 4$ rational surface for EAST discharge 52 340 with toroidal rotation. The amplitude of the RMP is adjusted by 5 kAt (blue), 10 kAt (red), and 20 kAt (green). The hexagrams along the vertical axis mark the amplitudes of the resonant $m/n = 4/1$ harmonic in vacuum for each case.

However, the artificial toroidal rotation speed is constrained to be sub-sonic. Under these conditions, the inertial force on the equilibria due to toroidal rotation is less than one percent of the entire pressure gradient force and is not included in the governing equations of the CLTx code initially. The same considerations are taken for discharges 52 340 and 62 558 discussed below.

Time evolutions of resonant harmonics $b_{m,n}^r$ driven by the $n = 1$ RMP for the equilibrium of discharge 52 340 with toroidal rotation are shown in figure 2(a). Nonlinear effects in the pedestal region ($m \geq 5, n = 1$) are still limited even if we artificially choose the large resistivity $\eta_0 = 5 \times 10^{-7}$ that is about two orders of magnitude larger than the experimental value. But, there is a significant difference for the unstable $m/n = 1/1$ kink mode between the linear and nonlinear simulations. Due to nonlinear mode coupling, the kink mode becomes saturated after $2100\tau_A$. These results suggest that nonlinear effects are not important before the internal kink instability begins to play a role in the overall plasma dynamics, although it should be noted that the islands overlap condition $|\partial\zeta_r/\partial r| < 1$ [5, 42] is not satisfied in the pedestal after considering the plasma response [33].

Figure 2(b) shows the simulation results for discharge 52 340 without the toroidal rotation. No saturation for any harmonic is observed in the linear simulation without toroidal rotation. While in the nonlinear case, the $m/n = 1/1$ kink mode becomes saturated as expected due to nonlinear mode coupling, which also leads to the reduction of higher harmonics ($m \geq 2, n = 1$).

The second set of simulations with EFIT reconstructed equilibrium for EAST discharge 62 585 at 3800 ms [57] is carried out both with and without the toroidal rotation. All parameters and the RMP configurations are the same as those in the preceding simulations. The safety factor profile of discharge

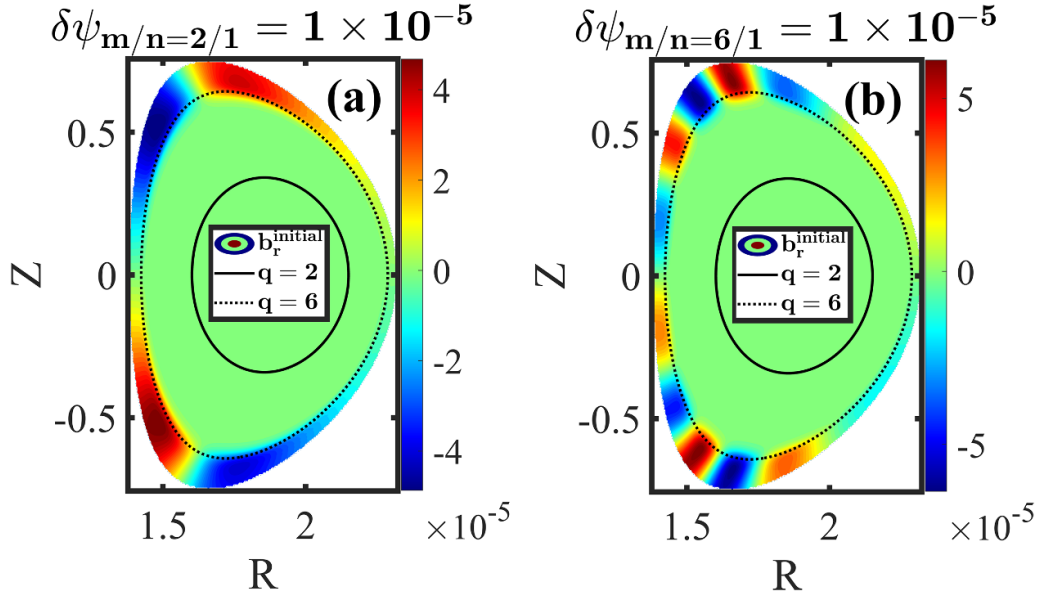


Figure 5. Initial perturbations of the radial magnetic field with $\delta\psi_{m,n} = 1 \times 10^{-5}$ from (a) the $m/n = 2/1$ RMP and (b) the $m/n = 6/1$ RMP. The rational surfaces of $q = 2$ and $q = 6$ are marked out by solid and dotted lines, respectively.

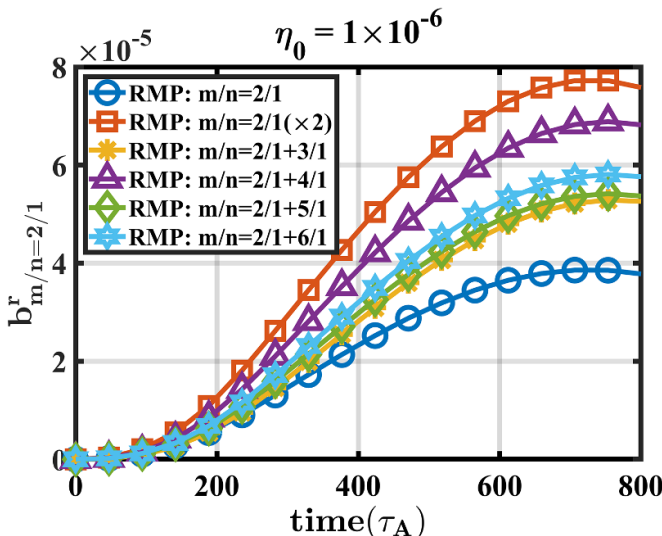


Figure 6. Time evolutions of $b_{m/n=2/1}^r$ at $q = 2$ rational surface with different harmonic compositions of RMP. The double-harmonic-RMP is the combination of the $m/n = 2/1$ harmonic and an extra harmonic ($m \geq 2$) with the same amplitude ($\delta\psi_{m,n} = 2 \times 10^{-5}$).

62 585 is monotonous with $q_{\min} = 1.59$ and $q_{95} = 4.87$ as shown in figure 1. The toroidal rotation profile of discharge 52 340 in figure 1 is artificially added in the static equilibrium of discharge 62 585 due to the lack of a self-consistent rotation profile. The results of discharge 62 585 in figures 2(c) and (d) show similar tendencies compared to those of discharge 52 340. All resonant harmonics with high poloidal mode numbers ($m \geq 3, n = 1$) become saturated both with and without toroidal rotation in both the linear and nonlinear simulations. Uniquely, the lowest resonant $m/n = 2/1$ tearing mode exhibits a continuous growth (the oscillation of its

amplitude is due to the mode rotating with the toroidal flow) in its linear simulation, while in the nonlinear simulation, this mode becomes saturated due to the generation of the $n = 0$ zonal component through nonlinear mode coupling. Figure 3 clearly shows that the resonant $m/n = 2/1$ tearing mode also exhibits a continuous growth if the $n = 0$ zonal component is artificially filtered out in the nonlinear simulation of CLTx. Similar results about the importance of $n = 0$ zonal component on the saturation of a tearing mode have been reported previously by CLT simulations [60, 61].

Through the comparison between both the EAST discharge 52 340 and 62 585, it is found that nonlinear effects are not important in the pedestal region until the internal MHD instabilities play the role (the $m/n = 1/1$ kink mode for discharge 52 340 and the $m/n = 2/1$ tearing mode for discharge 62 585). The toroidal plasma rotation [29], on the other hand, plays an effective role in shielding RMP penetration. But the nonlinear couplings lead to a significant difference in the dynamic evolutions of the internal MHD instabilities. Especially, the saturation of both the internal MHD instabilities and the whole system is not achieved until the nonlinear terms are retained. Thus, the importance of nonlinearities in the core plasma, the validity of the linearized MHD model in the pedestal region, and the effectiveness of toroidal plasma rotation on screening RMP penetration are demonstrated by comparing these two EAST discharges.

Similar saturated time-independent solutions for stable equilibria were reported in the linearized MHD simulations carried out with the M3D-C¹ code [39]. However, in our simulations of unstable equilibria with the toroidal rotation, the linearly saturated solutions for the $n = 1$ RMP are obtained for the harmonics with $m \geq 2$ in discharge 52 340 and $m \geq 3$ in discharge 62 585 with the presence of toroidal rotation. The same saturated results for high harmonics obtained in both linear and nonlinear simulations with the toroidal rotation further

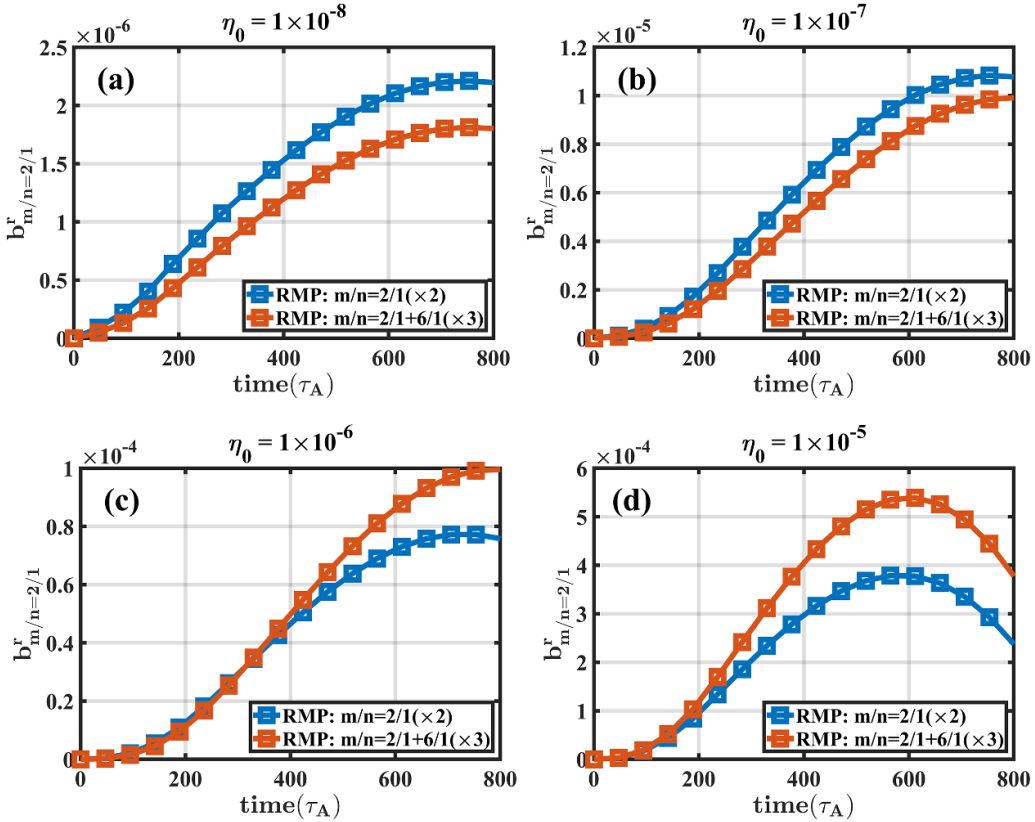


Figure 7. Time evolutions for amplitudes of $b_{m/n=2/1}^r$ at the $q = 2$ rational surface with different harmonic compositions of RMP. The results from the single-harmonic-RMP ($\delta\psi_{2,1} = 4 \times 10^{-5}$) are plotted using blue lines, while red lines represent results from the double-harmonic-RMP ($\delta\psi_{2,1} = 2 \times 10^{-5}$ and $\delta\psi_{6,1} = 6 \times 10^{-5}$). The resistivity used in each simulation is (a) $\eta_0 = 10^{-8}$, (b) $\eta_0 = 10^{-7}$, (c) $\eta_0 = 10^{-6}$, and (d) $\eta_0 = 10^{-5}$, respectively.

demonstrate the validity of the linear model used in the previous researches of the MARS-F and CLTx code [3, 33].

With different amplitudes of RMP $I_{\text{coil}} = 5$ kAt, 10 kAt, and 20 kAt, the time evolutions of the $m/n = 4/1$ harmonic at the $q = 4$ rational surface for EAST discharge 52 340 with the toroidal rotation are given in figure 4. With the relatively large resistivity $\eta_0 = 5 \times 10^{-7}$ (about two orders of magnitude larger than the experimental value), the shielding effects due to plasma response are almost identical for all cases with the shielding ratio ($b_{\text{response}}^r / b_{\text{vacuum}}^r$) approaching approximately 60%. Meanwhile, the overall qualitative evolutions among all cases are almost identical, that is, the modes for all cases become saturated after $3000\tau_A$. The saturation amplitude of the high resonant harmonic with plasma response is linearly proportional to the intensity of the vacuum RMP. Also, the increase of the RMP intensity does not lead to the breakdown of high resonant harmonics.

4. Toroidal effect on penetration of RMP

In this section, we mainly focus on the toroidal effect on penetration of RMP in the interior resonant surfaces. Thus, the SOL region is not included in this study. In order to reduce the impact of boundary treatment, the safety factor for discharge 52 340 is truncated to a finite value at the plasma boundary and

the $q = 6$ rational surface is slightly shifted inward. The reconstructed equilibrium from the QSOLVER code [62] is given by the red line in figure 9. The RMP field is applied inside the plasma boundary where the generalized poloidal angle θ_s can be defined accurately. Usually, RMP fields generated by realistic coils contain multiple resonant and non-resonant harmonics, and the penetration of a specific harmonic could be influenced by others [25, 50]. In this section, instead of the RMP fields directly calculated from the realistic coils, we choose the RMP to be artificially composited with different harmonics of the perturbed magnetic flux $\delta\psi_{\text{RMP}}$ as follows,

$$\delta\psi_{\text{RMP}} = \sum_{m,n} \delta\psi_{m,n} \cos(m\theta_s(\psi_n) + n\phi) (1 + \tanh((\psi_n - \psi_0)/d_{\text{RMP}}))/m, \quad (7)$$

where $\delta\psi_{m,n}$ is on the order of 10^{-5} , corresponding to currents of several kiloamperes (kA), ψ_n is the normalized poloidal flux, $\psi_0 = 0.90$, and $d_{\text{RMP}} = 0.02$. The initial distributions of radial magnetic perturbations with $\delta\psi_{m,n} = 1 \times 10^{-5}$ from the $m/n = 2/1$ and $m/n = 6/1$ RMPs are shown in figure 5.

With varying combinations of different RMP harmonics, the response of the radial perturbation of the resonant magnetic field $b_{m/n=2/1}^r$ at the $q = 2$ rational surface is investigated. The reason for choosing the $q = 2$ surface is that the penetration

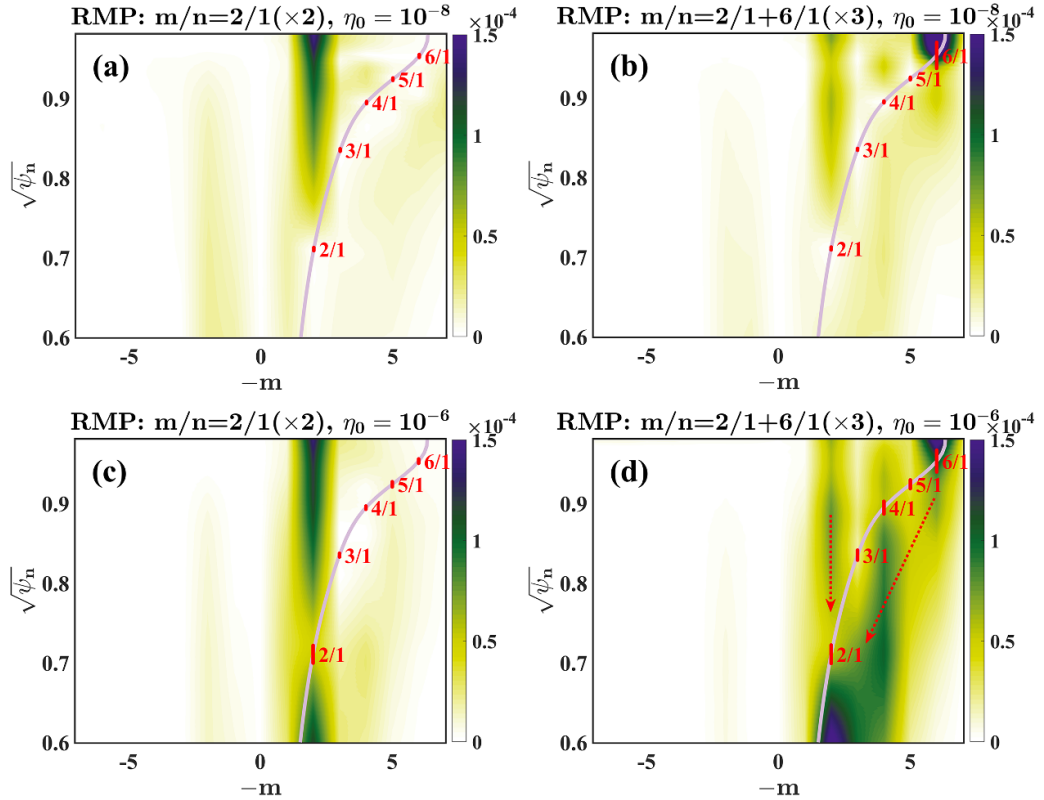


Figure 8. The radial distributions of the $b_{n=1}^r$ spectra at $t = 423\tau_A$ for the small resistivity $\eta_0 = 10^{-8}$ in the upper panel (a) the single-harmonic-RMP ($\delta\psi_{2,1} = 4 \times 10^{-5}$) and (b) the double-harmonic-RMP ($\delta\psi_{2,1} = 2 \times 10^{-5}$, $\delta\psi_{6,1} = 6 \times 10^{-5}$) as well as for the large resistivity $\eta_0 = 10^{-6}$ in the lower panel (c) the single-harmonic-RMP ($\delta\psi_{2,1} = 4 \times 10^{-5}$) and (d) the double-harmonic-RMP ($\delta\psi_{2,1} = 2 \times 10^{-5}$, $\delta\psi_{6,1} = 6 \times 10^{-5}$).

mechanisms for different harmonics should be qualitatively consistent and the spectrum analysis is more accurate for lower harmonics. In the first subsection below, we discuss the simulation results of the single-harmonic-RMP and the double-harmonic-RMP, in which the different roles played by resonant and non-resonant components will be illustrated. In the second subsection, the poloidal harmonic filtering analysis and the multiple-harmonic-RMP simulation results are presented to confirm the importance of poloidal harmonic coupling on RMP penetration.

4.1. Single and double harmonic RMPs

In this subsection, the single-harmonic-RMP is chosen to be two different amplitudes with $\delta\psi_{2,1} = 2 \times 10^{-5}$ and $\delta\psi_{2,1}(\times 2) = 4 \times 10^{-5}$ while the double-harmonic-RMP consists of the $m/n = 2/1$ harmonic and another higher m harmonic ($m > 2$, $n = 1$) with the same amplitude $\delta\psi_{m,n} = 2 \times 10^{-5}$. A large resistivity $\eta_0 = 10^{-6}$ (about two orders of magnitude larger than the experimental value) is used and all simulations are carried out based on the fully nonlinear simulation code CLT. Figure 6 shows time evolutions of $b_{m/n=2/1}^r$ with two different harmonic compositions of RMP. It is evident that, compared with the single $m/n = 2/1$ harmonic RMP with $\delta\psi_{2,1} = 2 \times 10^{-5}$, an extra higher harmonic ($m > 2$) in RMP results in a larger tearing mode response at the $q = 2$

rational surface. In particular, the amplitude of $b_{m/n=2/1}^r$ under the $m/n = 2/1 + 4/1$ RMP is the largest among all cases with higher harmonic superposition ($m > 2$), but still remains less than that of the $m/n = 2/1 (\times 2)$ RMP with $\delta\psi_{2,1}(\times 2) = 4 \times 10^{-5}$. Consequently, the higher harmonics ($m > 2$) of the RMP could generate considerable driving effects at the $q = 2$ rational surface.

To further understand how the higher harmonics enhance the tearing mode response at the $q = 2$ rational surface, another comparison study is carried out by using different values of the resistivity (ranging from 10^{-8} to 10^{-5}) based on two sets of RMP configuration with (a) the single-harmonic-RMP $\delta\psi_{2,1} = 4 \times 10^{-5}$ and (b) the double-harmonic-RMP $\delta\psi_{2,1} = 2 \times 10^{-5}$ and $\delta\psi_{6,1} = 6 \times 10^{-5}$, respectively. A relatively large $m = 6$ component is added in the double-harmonic-RMP to strengthen its driving effect. The time evolutions of $b_{m/n=2/1}^r$ at the $q = 2$ surface with different RMP configurations are plotted in figure 7. For a small resistivity $\eta_0 = 10^{-8}$ (close to the experimental value) as shown in figure 7(a), the amplitude of $b_{m/n=2/1}^r$ is smaller in the double-harmonic-RMP than in the single-harmonic-RMP, which suggests that the driving effect of the $m = 6$ harmonic at the $q = 2$ rational surface is relatively weak. However, the driving effect from the higher harmonic becomes more important with increasing the resistivity. When the resistivity increases to $\eta_0 = 10^{-6}$ (about two orders of magnitude larger than the experimental value) as

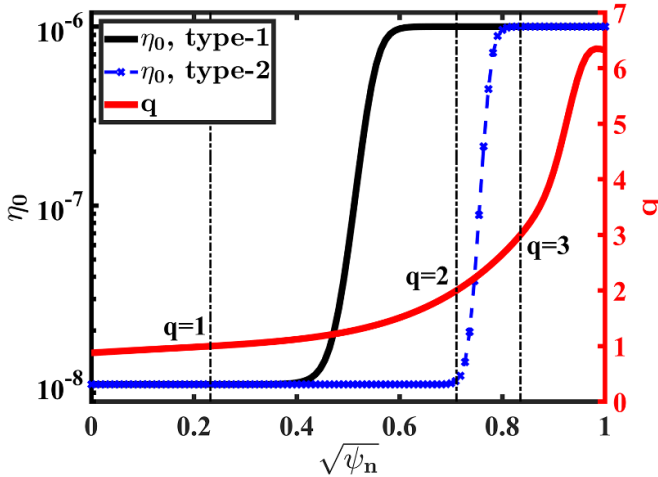


Figure 9. Profiles of the safety factor (red line) reconstructed for discharge 52 340 with the QSOLVER code and the two different types of resistivity η_0 distributions. Type-1 (black line): the small resistivity value ($\eta_0 = 10^{-8}$) is applied inside the $q = 1$ rational surface, but the resistivity in the outer region ($q > 1$) remains at a high level ($\eta_0 = 10^{-6}$) and Type-2 (blue line): the small resistivity value ($\eta_0 = 10^{-8}$) is applied inside the $q = 2$ rational surface, but the resistivity in the outer region ($q > 2$) keeps at a high level ($\eta_0 = 10^{-6}$).

shown in figure 7(c), the amplitude of $b_{m/n=2/1}^r$ in the double-harmonic-RMP exceeds that of the single-harmonic-RMP. However, it should be noted that the case with low resistivity $\eta_0 = 10^{-8}$ is most relevant to the experiment. The results suggest that although the $m/n = 6/1$ harmonic in RMP could generate considerable tearing response at the $q = 2$ rational surface (especially with the larger resistivity), the driving effect of the $m/n = 2/1$ harmonic in RMP is still more effective than that of the $m/n = 6/1$ harmonic with the experimental value of the resistivity.

Figure 8 exhibits the $b_{n=1}^r$ spectra corresponding to the cases in figures 7(a) and (c). For the low resistivity $\eta_0 = 10^{-8}$ close to the experimental value, as shown in the upper panel of figure 8, the penetration depth of the $m = 2$ harmonic is limited outside the $q = 2$ rational surface for both types of RMPs. The $m = 6$ harmonic vanishes quickly before reaching the $q = 2$ surface. Consequently, the resulting $m = 2$ and $m = 6$ perturbations from the double-harmonic-RMP are almost independent of each other, and the $b_{m/n=2/1}^r$ is mainly driven by the $m = 2$ harmonic of the RMP. The spectrum is consistent with that shown in figure 7(a), where the amplitude of $b_{m/n=2/1}^r$ from the double-harmonic-RMP is lower than that from the single-harmonic-RMP. However, when the resistivity increases to $\eta_0 = 10^{-6}$ (about two orders of magnitude larger than the experimental value), the penetration depths from both types of RMP are significantly boosted, which suggests that the large resistivity can largely reduce the current shielding and enhance the penetration of RMPs. Meanwhile, the results from the double-harmonic-RMP also become completely different. Due to the toroidal effect, the strong $m = 6$ harmonic in RMP generates a sequence of lower harmonics from $m = 5$ to $m = 2$ and propagates inward to

the central plasma region. The longest arrow in figure 8(d) indicates the inward propagation direction of RMP from the $m = 6$ harmonic to the $m = 2$ harmonic due to the poloidal harmonic coupling. After successful penetration by the higher harmonic, the considerable $m = 3$ and $m = 4$ components are generated at the $q = 2$ rational surface, which could indirectly drive $b_{m/n=2/1}^r$. In addition, the $b_{m/n=2/1}^r$ component inside the $q = 2$ rational surface also becomes much larger than that of the single-harmonic-RMP. Therefore, for the double-harmonic-RMP, the inside and outside resonant driving ($m = 2$) and the non-resonant driving ($m > 2$) together result in the final amplitude of $b_{m/n=2/1}^r$ to exceed that of the single-harmonic-RMP, even though the direct $m = 2$ driving strength from the double-harmonic-RMP is only a half of the single-harmonic-RMP.

The influences from the intrinsic kink and tearing instabilities ($m/n = 1/1$ resistive kink mode and $m/n = 2/1$ tearing mode) on the RMP penetration are further examined by using two types of artificial resistivity distributions as shown in figure 9. With the type-1 distribution, the small resistivity $\eta_0 = 10^{-8}$ close to the experimental value is applied inside the $q = 1$ rational surface to reduce the growth rate of the $m/n = 1/1$ resistive kink mode, while the resistivity in the outer region ($q > 1$) remains at a high level ($\eta_0 = 10^{-6}$, about two orders of magnitude larger than the experimental value). As shown in figure 10, the only difference resulting from the type-1 resistivity distribution is that the $b_{m/n=1/1}^r$ at the $q = 1$ rational surface becomes much weaker because magnetic reconnection is suppressed due to the small resistivity. In contrast, outside the $q = 1$ rational surface, the global mode structures of $b_{m/n}^r$ are almost identical between these two cases. Consequently, the fast growth of the $m/n = 1/1$ harmonic is the result of the external driving process rather than the intrinsic resistive kink instability.

The type-2 resistivity distribution as shown in figure 9 is that the resistivity inside the $q = 2$ rational surface is set to be $\eta_0 = 10^{-8}$, close to the experimental value while the resistivity outside the $q = 2$ rational surface is chosen to be $\eta_0 = 10^{-6}$, about two orders of magnitude larger than the experimental value. With the type-2 distribution of the resistivity, the penetration properties of the single-harmonic-RMP and the double-harmonic-RMP become totally different. Firstly, due to the generation of the screen currents, a strong shielding effect is observed in the mode structures of $b_{m/n=2/1}^r$ in figure 11(a) and δE_ϕ in figure 12(a). Thus, the penetration of the single-harmonic-RMP is blocked at the $q = 2$ rational surface, and the amplitude of the $b_{m/n=2/1}^r$ component inside the $q = 2$ surface is much weaker than that outside the surface. In contrast, with the double-harmonic-RMP applied as shown in figure 11(b), a series of intermediate non-resonant harmonics (m from 3 to 5) are greatly generated across the entire space. As a result, with the double-harmonic-RMP, the penetrated $b_{m/n=2/1}^r$ component inside the $q = 2$ surface is comparable with that outside the surface. In consequence, with the indirect driving from non-resonant harmonics ($m > 2$) at the rational surface and the direct driving from resonant harmonic ($m = 2$) both inside and outside,

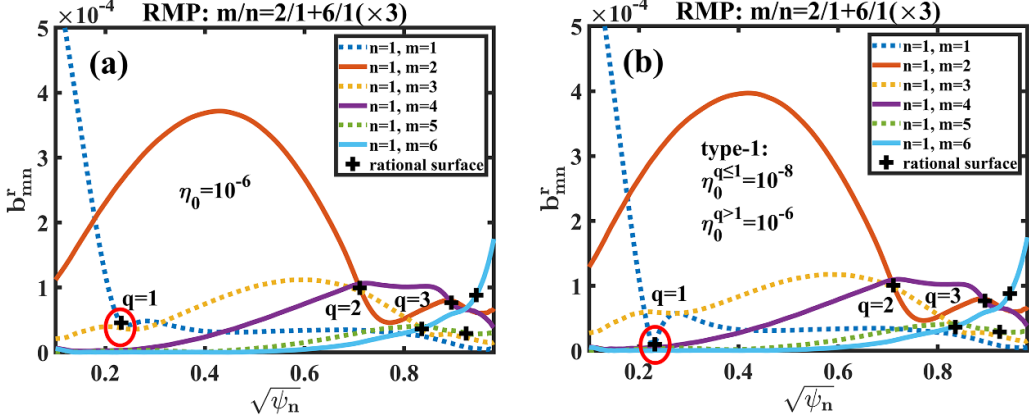


Figure 10. The radial structures of $b_{m/n}^r$ at $t = 800\tau_A$ with the double-harmonic-RMP ($\delta\psi_{2,1} = 2 \times 10^{-5}$, $\delta\psi_{6,1} = 6 \times 10^{-5}$) for (a) the uniform η_0 resistivity distribution with $\eta_0 = 10^{-6}$ and (b) the type-1 resistivity distribution with $\eta_0^{q \leq 1} = 10^{-8}$ and $\eta_0^{q > 1} = 10^{-6}$.

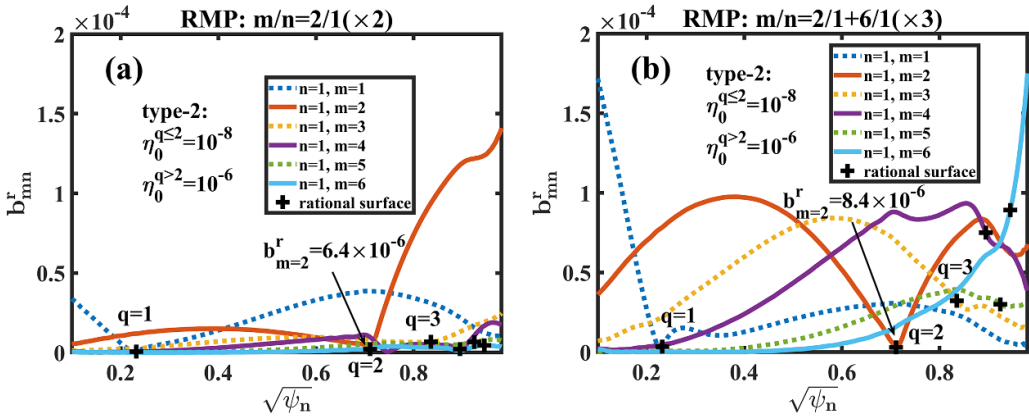


Figure 11. The radial structures of $b_{m/n}^r$ at $t = 800\tau_A$ with the type-2 resistivity distribution ($\eta_0^{q \leq 2} = 10^{-8}$ and $\eta_0^{q > 2} = 10^{-6}$) for (a) the single-harmonic-RMP ($\delta\psi_{2,1} = 4 \times 10^{-5}$) and (b) the double-harmonic-RMP ($\delta\psi_{2,1} = 2 \times 10^{-5}$, $\delta\psi_{6,1} = 6 \times 10^{-5}$).

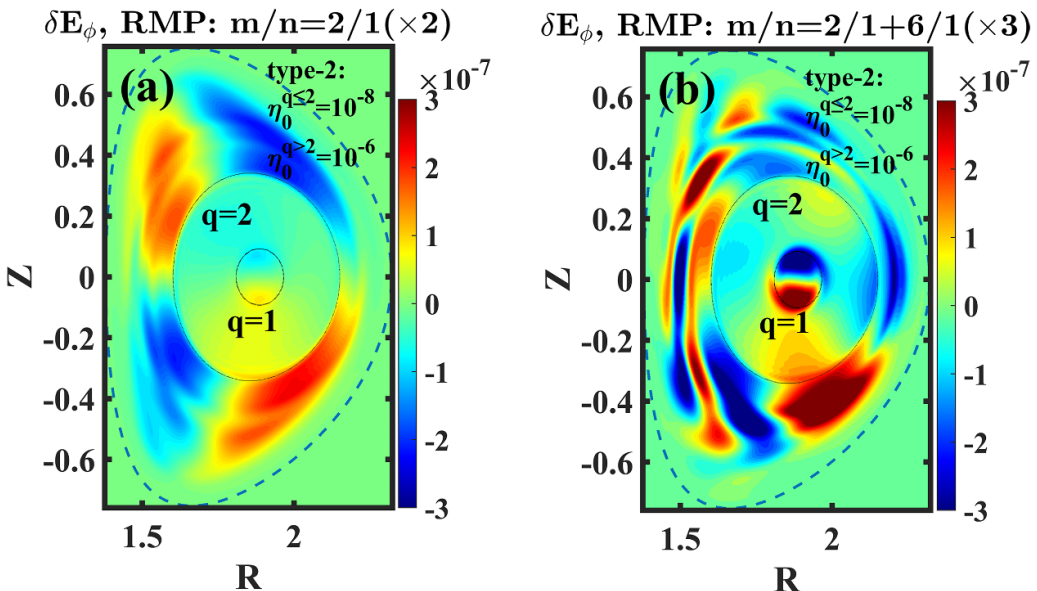


Figure 12. The mode structures of δE_ϕ at $t = 800\tau_A$ with the type-2 resistivity distribution, $\eta_0^{q \leq 2} = 10^{-8}$ and $\eta_0^{q > 2} = 10^{-6}$ for (a) the single-harmonic-RMP ($\delta\psi_{2,1} = 4 \times 10^{-5}$) and (b) the double-harmonic-RMP ($\delta\psi_{2,1} = 2 \times 10^{-5}$, $\delta\psi_{6,1} = 6 \times 10^{-5}$).

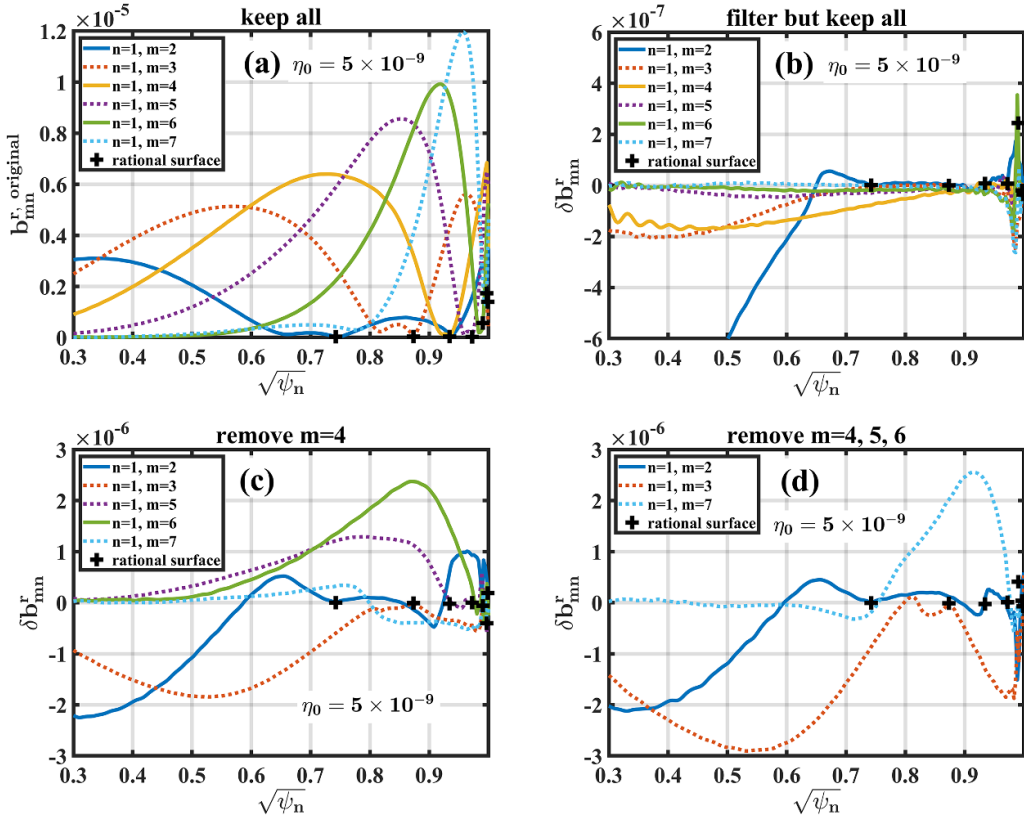


Figure 13. (a) The original radial structures of $b_{m,n}^r$ in the $n = 1$ RMP simulation for EAST. The difference of each harmonic ($\delta b_{m,n}^r = b_{m,n}^r - b_{m,n}^{r,\text{original}}$) of two runs with and without (b) employing interpolations and Fourier transformations (all harmonics are retained), (c) artificially removing the $m = 4$ harmonic, and (d) artificially removing the $m = 4-5-6$ harmonics.

the amplitude of $b_{m/n=2/1}^r$ at the $q = 2$ surface far exceeds that of the single-harmonic-RMP, even though the external $m = 2$ driving strength in the single-harmonic-RMP case is doubled. Meanwhile, as shown in figure 12(b), the $m/n = 1/1$ perturbation resulting from the double-harmonic-RMP penetrates deeply into the central core region, and consequently, a strong kink mode is excited inside the $q = 1$ rational surface.

In Tokamaks, the couplings between the various Fourier harmonics are mainly resulted from two mechanisms. The first one is the poloidal harmonic coupling associated with the toroidal effect, which is mainly caused by the non-uniformity of the toroidal magnetic field B_ϕ . With the dependence of $B_\phi \propto R^{-1} \propto (1 + \epsilon \cos \theta)^{-1} \approx (1 - \epsilon \cos \theta)$, ($\epsilon = r/R_0$ is the inverse aspect ratio; R_0 and r are, respectively, the major radius of the magnetic axis and the minor radius), any perturbation with the poloidal mode number m could generate the $m \pm 1$ sidebands. In other words, because the poloidal mode number is not a good quantum number [63], all harmonics with different poloidal mode numbers are coupled together intrinsically in both linear and nonlinear simulations. The influence of poloidal harmonic coupling on RMP penetration has been mentioned in previous researches as well [25, 33, 50]. In addition to the poloidal harmonic coupling, the second coupling mechanism is the toroidal harmonic coupling due to nonlinear effects. As for this part of the results, the poloidal harmonic coupling plays the major role.

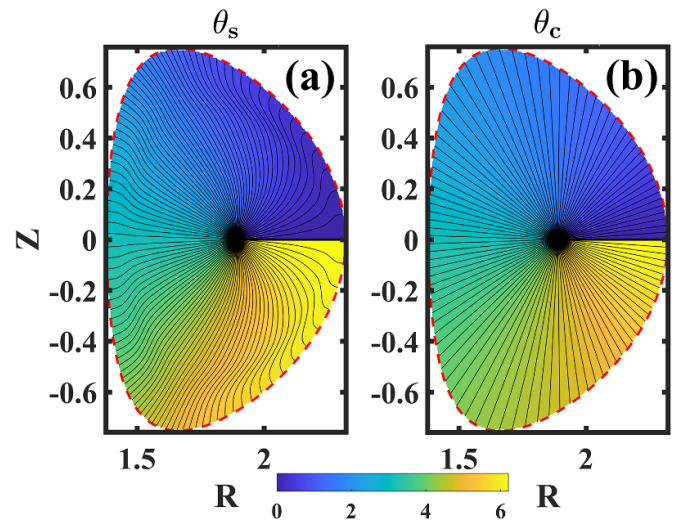


Figure 14. The distributions of (a) the generalized poloidal angle θ_s of basic straight field line coordinate and (b) the uniformly distributed poloidal angle θ_c .

4.2. Poloidal harmonic filtering analysis and the multiple-harmonic-RMP

A supplementary study concerning the toroidal effect on RMP penetration has been carried out using poloidal filtering analysis. The filtering analysis is applied in the linear EAST RMP simulation, with the same parameters as

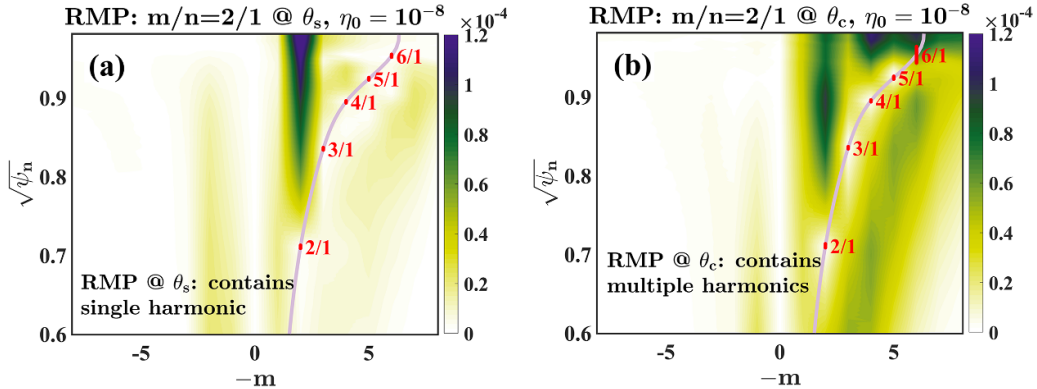


Figure 15. The radial distributions of the $b_{n=1}^r$ spectra at $t = 423\tau_A$ for (a) the RMP depending on θ_s (contains the single $m/n = 2/1$ harmonic) and (b) the RMP depending on θ_c (contains multiple harmonics).

those reported previously [33]. The resistivity is chosen to be the experimental value $\eta_0 = 5 \times 10^{-9}$. The SOL has been retained and the vacuum RMP field is calculated based on the realistic RMP coils. Because the Cartesian grids in the poloidal section are used in the CLTx code, poloidal filtering analysis demands two coordinate transformations with interpolations among Cartesian grids and magnetic flux grids inside the plasma boundary for carrying out the Fourier transformations while an asymptotic transition is applied between the plasma and SOL regions for numerical continuity. The original radial structure (without any poloidal filtering analysis) of $b_{m,n}^{r,\text{original}}$ under the $n = 1$ EAST RMP is plotted in figure 13(a). To analyze the numerical errors resulting from the interpolations from coordinate transformations, we conducted a controlling simulation by employing the interpolations and Fourier transformations while all harmonics are retained in the inverse Fourier transformation. The results shown in figure 13(b) indicate that the numerical errors due to these processes only lead to a limited decline of the $m = 2$ harmonic, but the errors' influences on higher harmonics ($m \geq 3$) can be ignorable ($|\delta b_{m,n}^r / b_{m,n}^{r,\text{original}}| < 5\%$, $\delta b_{m,n}^r = b_{m,n}^r - b_{m,n}^{r,\text{original}}$). After we removed the $m = 4$ component in the inverse Fourier transformation, the global amplitude of $m = 3$ is greatly reduced by about half as shown in figure 13(c). Next, as shown in figure 13(d), after we removed more intermediate harmonics ($m = 4, 5, 6$), the amplitude of the global $m = 3$ perturbation is further reduced. Another interesting phenomenon is that after removing the intermediate harmonics in the simulation, the amplitudes of the higher harmonics exhibit an enhancement, examples of which can be seen for the $m = 5, 6$ harmonics in figure 13(c), and the $m = 7$ harmonic in figure 13(d). By removing the intermediate harmonics, the inward propagation channel from higher harmonics to lower harmonics is blocked, this results in amplitude decline of the inside lower harmonics and flux accumulation at the outside higher harmonics.

Based on the above results with the experimental resistivity ($\eta_0 = 5 \times 10^{-9}$) about effects of the poloidal harmonic coupling, it is suggested that, in comparison with the single-harmonic-RMP, the multiple-harmonic-RMP could efficiently drive the development of MHD instabilities in the central

plasma region. Also, in experiments, the generalized poloidal angle θ_s is hard to determine during the discharge. An RMP with a single dominant harmonic produced by realistic coils in the experiment usually contains multiple sideband harmonics. Therefore, a set of simulations is carried out with the low resistivity close to the experimental value ($\eta_0 = 1 \times 10^{-8}$) to investigate roles of the multiple-harmonic-RMP on dynamic process of the tearing mode instabilities. The simulations are carried out with the equilibrium shown in figure 9 and the RMPs are applied inside the plasma boundary with the formula of equation (7). The multiple-harmonic-RMP is implemented by changing the generalized poloidal angle θ_s of the basic straight field line coordinate in equation (7) into the uniformly distributed poloidal angle θ_c (θ_c can be defined simply in experiments). Note that magnetic field lines are no longer straight in the $\theta_c - \phi$ plane. The distributions of θ_s and θ_c are shown in figures 14(a) and (b), respectively. The RMPs with $\delta\psi_{2,1} = 4 \times 10^{-5}$ applied with the θ_s or θ_c dependence produce different radial distributions of the $b_{n=1}^r$ spectra as shown in figures 15(a) and (b). The RMP depending on θ_s contains only the single $m/n = 2/1$ harmonic as shown in figure 15(a) and is named as the single-harmonic-RMP. While the latter one with the θ_c dependence contains multiple harmonics ranging from $m = 2 \sim 7$ as shown in figure 15(b), which is similar to the experimental situation, and is named as the multiple-harmonic-RMP. Apparently, the multiple-harmonic-RMP with the θ_c dependency creates the multiple harmonic perturbations at the pedestal region, which results in a large enhancement of the non-resonant components ($|m| > |nq|$) at the $q = 2$ rational surface due to the successful penetration of high harmonic perturbations. Consequently, the resulted tearing mode response at the $q = 2$ rational surface from the multiple-harmonic-RMP is much larger than that from the single-harmonic-RMP as shown by figure 16.

Consequently, the poloidal harmonic filtering analysis and the multiple-harmonic-RMP simulation with the experimental low resistivity ($\eta_0 \approx 10^{-8}$) indicate that multiple-harmonic-RMP can largely help the low- m harmonics penetrate into the core region through the poloidal harmonic coupling.

From these present simulations, we also find that nonlinear effects on the inward penetration of higher harmonic RMPs

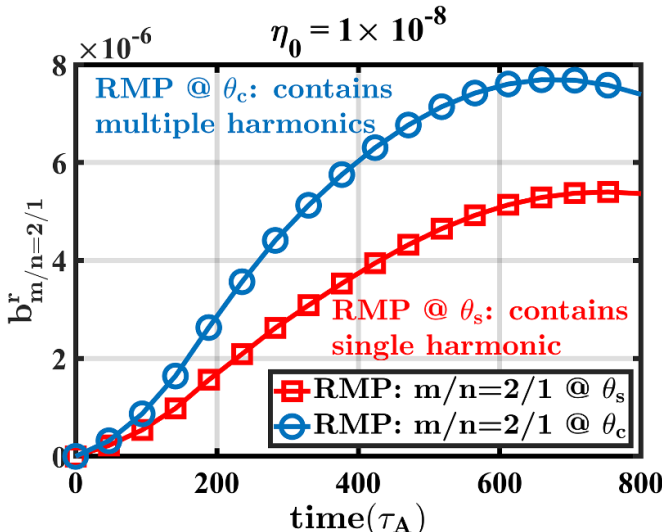


Figure 16. Time evolutions for amplitudes of $b_{m/n=2/1}^r$ with different RMPs: the red squares for the RMP depending on θ_s (contains the single $m/n = 2/1$ harmonic) and the blue circles for the RMP depending on θ_c (contains multiple harmonics).

are negligible due to the overlap condition $|\partial\zeta_r/\partial r| < 1$ being well satisfied. Thus, the linear simulations also give the same results as figure 16. Nevertheless, nonlinear effects may still be important when the magnetic islands grow large enough to affect the adjacent rational surfaces.

5. Conclusion and discussion

In the present paper, the CLTx code is used to study the $n = 1$ RMP penetration. The comparison study between the linear and nonlinear modeling indicates that with the presence of toroidal plasma rotation, the final steady state or saturated state for high resonant harmonics could be obtained in the initial value simulations of the CLTx code using the linearized MHD equations. Thus, nonlinear effects are negligible since the magnetic islands evolve into a linearly saturated state due to plasma response and shielding. With both the experimental resistivity and the artificially amplified resistivity (by two orders of magnitude), the nonlinear simulations for discharge 52 340 give the same results for rational surfaces around the pedestal as the linear simulations [33]. The consistency between linear and nonlinear simulations of CLTx suggests that the linearized MHD model with the experimental resistivity may be acceptable for the RMP study if the toroidal rotation is relatively large. However, our results indicate that the linearized MHD model is broken down for the cases without the toroidal rotation. This is because, without plasma rotation and nonlinear effects, the low- m resonant harmonics in the core region give evolution dynamics with continuous growth where the final saturated state is not obtained unless the nonlinear terms are included. Consequently, the linearized model leads to the failure of predicting the shielding effect by plasma response. Therefore, for future Tokamaks with zero or low-speed toroidal rotation, such as ITER [64] as well, the

inclusion of nonlinear effects will probably be necessary for the RMP study, even though the resistivity could be lower than the present experimental devices.

The simulations focusing on the toroidal effect in RMP penetration demonstrate that poloidal harmonic coupling [25, 50] is a consequence of the toroidal effect instead of nonlinear effects. With a low resistivity close to the experimental value, the single-harmonic-RMP is hard to penetrate the mode rational surface in the inner region because of the plasma screening effects, resulting in a truncation of the radial mode structure. On the other hand, the non-resonant components in the multiple-harmonic-RMP could largely reduce the plasma shielding, and thus play a positive role in the RMP penetration through the poloidal harmonic coupling. Consequently, with the inclusion of higher harmonics in RMP, the penetration by lower harmonics could become larger. The removal of the intermediate harmonics leads to breaking down the poloidal harmonic coupling and subsequently prevents the outside higher harmonics from penetrating into the core region, which results in an amplitude decrease (increase) of the inner lower (outer higher) harmonics. Finally, the observed mode coupling is mainly caused by the inhomogeneity of the toroidal equilibrium magnetic field rather than by the nonlinear effects. Consequently, nonlinear effects are unimportant for mode couplings when the toroidal effect dominates. This indicates a possible explanation for the similar results obtained by both the linear and nonlinear simulations.

Acknowledgments

This work was supported by the Special Project on High-performance Computing under the National Key R&D Program of China Grant No. 2016YFB0200603, the National Natural Science Foundation of China under Grant Nos. 11775188 and 11835010, and the Fundamental Research Fund for Chinese Central Universities.

ORCID iDs

- H W Zhang <https://orcid.org/0000-0003-1342-5756>
Z W Ma <https://orcid.org/0000-0001-6199-9389>
W Zhang <https://orcid.org/0000-0001-5859-6298>

References

- [1] Zohm H 1996 Edge localized modes (ELMs) *Plasma Phys. Control. Fusion* **38** 105–128
- [2] Wagner F *et al* 1982 Regime of improved confinement and high-beta in neutral-beam-heated divertor discharges of the ASDEX tokamak *Phys. Rev. Lett.* **49** 1408–12
- [3] Yang X, Sun Y, Liu Y, Gu S, Liu Y, Wang H, Zhou L and Guo W 2016 Modelling of plasma response to 3D external magnetic field perturbations in EAST *Plasma Phys. Control. Fusion* **58** 114006
- [4] Sun Y *et al* 2016 Nonlinear transition from mitigation to suppression of the edge localized mode with resonant magnetic perturbations in the EAST tokamak *Phys. Rev. Lett.* **117** 115001

- [5] Liu Y Q, Ham C J, Kirk A, Li L, Loarte A, Ryan D A, Sun Y, Suttrop W, Yang X and Zhou L 2016 ELM control with RMP: plasma response models and the role of edge peeling response *Plasma Phys. Control. Fusion* **58** 114005
- [6] Suttrop W *et al* 2013 Mitigation of edge localised modes with magnetic perturbations in ASDEX upgrade *Fusion Eng. Des.* **88** 446–53
- [7] Suttrop W *et al* 2011 Studies of edge localized mode mitigation with new active in-vessel saddle coils in ASDEX upgrade *Plasma Phys. Control. Fusion* **53** 124014
- [8] Suttrop W *et al* 2011 First observation of edge localized modes mitigation with resonant and nonresonant magnetic perturbations in ASDEX upgrade *Phys. Rev. Lett.* **106** 225004
- [9] Wade M R *et al* 2015 Advances in the physics understanding of ELM suppression using resonant magnetic perturbations in DIII-D *Nucl. Fusion* **55** 023002
- [10] Wingen A *et al* 2015 Connection between plasma response and resonant magnetic perturbation (RMP) edge localized mode (ELM) suppression in DIII-D *Plasma Phys. Control. Fusion* **57** 104006
- [11] Moyer R A *et al* 2017 Validation of the model for ELM suppression with 3D magnetic fields using low torque ITER baseline scenario discharges in DIII-D *Phys. Plasmas* **24** 102501
- [12] Evans T E *et al* 2006 Edge stability and transport control with resonant magnetic perturbations in collisionless tokamak plasmas *Nat. Phys.* **2** 419–23
- [13] Evans T E *et al* 2005 Suppression of large edge localized modes with edge resonant magnetic fields in high confinement DIII-D plasmas *Nucl. Fusion* **45** 595–607
- [14] Evans T E *et al* 2004 Suppression of large edge-localized modes in high-confinement DIII-D plasmas with a stochastic magnetic boundary *Phys. Rev. Lett.* **92** 235003
- [15] Ko W-H, Lee H H, Jeon Y M, Ida K, Lee J H, Yoon S W, Lee K D, Bae Y S, Oh Y K and Kwak J G 2014 Rotation characteristics during the resonant magnetic perturbation induced edge localized mode suppression on the KSTAR *Rev. Sci. Instrum.* **85** 11E413
- [16] In Y, Loarte A, Lee H H, Kim K, Jeon Y M, Park J-K, Ahn J-W, Park G Y, Kim M and Park H 2019 Test of the ITER-like resonant magnetic perturbation configurations for edge-localized mode crash suppression on KSTAR *Nucl. Fusion* **59** 126045
- [17] Jeon Y M *et al* 2012 Suppression of edge localized modes in high-confinement KSTAR plasmas by nonaxisymmetric magnetic perturbations *Phys. Rev. Lett.* **109** 035004
- [18] Kirk A *et al* 2013 Understanding edge-localized mode mitigation by resonant magnetic perturbations on MAST *Nucl. Fusion* **53** 043007
- [19] Kirk A, Liu Y, Nardon E, Tamain P, Cahyna P, Chapman I, Denner P, Meyer H, Mordijk S and Temple D 2011 Magnetic perturbation experiments on MAST L- and H-mode plasmas using internal coils *Plasma Phys. Control. Fusion* **53** 065011
- [20] Kirk A, Harrison J, Liu Y, Nardon E, Chapman I T and Denner P 2012 Observation of lobes near the X point in resonant magnetic perturbation experiments on MAST *Phys. Rev. Lett.* **108** 255003
- [21] Liang Y *et al* 2007 Active control of type-I edge-localized modes with n=1 perturbation fields in the JET tokamak *Phys. Rev. Lett.* **98** 265004
- [22] Boozer A H and Nuhrenberg C 2006 Perturbed plasma equilibria *Phys. Plasmas* **13** 102501
- [23] Boozer A H 2006 Perturbation to the magnetic field strength *Phys. Plasmas* **13** 044501
- [24] Nardon E, Bécout M, Huyssmans G and Czarny O 2007 Magnetohydrodynamics modelling of H-mode plasma response to external resonant magnetic perturbations *Phys. Plasmas* **14** 092501
- [25] Orain F *et al* 2017 Non-linear modeling of the plasma response to RMPs in ASDEX upgrade *Nucl. Fusion* **57** 022013
- [26] Liu F, Huijsmans G T A, Loarte A, Garofalo A M, Solomon W M, Snyder P B, Hoelzl M and Zeng L 2015 Nonlinear MHD simulations of Quiescent H-mode plasmas in DIII-D *Nucl. Fusion* **55** 113002
- [27] Bécoulet M *et al* 2014 Mechanism of edge localized mode mitigation by resonant magnetic perturbations *Phys. Rev. Lett.* **113** 115001
- [28] Orain F *et al* 2013 Non-linear magnetohydrodynamic modeling of plasma response to resonant magnetic perturbations *Phys. Plasmas* **20** 102510
- [29] Li L, Liu Y Q, Liang Y, Wang N, Luan Q, Zhong F C and Liu Y 2016 Screening of external magnetic perturbation fields due to sheared plasma flow *Nucl. Fusion* **56** 092008
- [30] Izzo V A and Joseph I 2008 RMP enhanced transport and rotational screening in simulations of DIII-D plasmas *Nucl. Fusion* **48** 115004
- [31] Pankin A Y, Bateman G, Brennan D P, Kritz A H, Kruger S, Snyder P B, Sovinec C and Team T N 2007 Modelling of ELM dynamics for DIII-D and ITER *Plasma Phys. Control. Fusion* **49** S63–S75
- [32] Bécoulet M *et al* 2012 Screening of resonant magnetic perturbations by flows in tokamaks *Nucl. Fusion* **52** 054003
- [33] Zhang H W, Ma Z W, Zhang W, Sun Y W and Yang X 2019 Penetration properties of resonant magnetic perturbation in EAST tokamak *Phys. Plasmas* **26** 112502
- [34] Xiao W W, Evans T, Tynan G, Yoon S, Jeon Y, Ko W, Nam Y and Oh Y 2017 Propagation dynamics associated with resonant magnetic perturbation fields in high-confinement mode plasmas inside the KSTAR tokamak *Phys. Rev. Lett.* **119** 205001
- [35] Sun Y *et al* 2016 Edge localized mode control using n=1 resonant magnetic perturbation in the EAST tokamak *Nucl. Fusion* **57** 036007
- [36] Xiao W W, Evans T E, Tynan G R and Eldon D 2016 Location of the first plasma response to resonant magnetic perturbations in DIII-D H-mode plasmas *Nucl. Fusion* **56** 064001
- [37] Lyons B C, Ferraro N M, Paz-Soldan C, Nazikian R and Wingen A 2017 Effect of rotation zero-crossing on single-fluid plasma response to three-dimensional magnetic perturbations *Plasma Phys. Control. Fusion* **59** 044001
- [38] Strauss H R, Sugiyama L, Park G Y, Chang C S, Ku S and Joseph I 2009 Extended MHD simulation of resonant magnetic perturbations *Nucl. Fusion* **49** 055025
- [39] Ferraro N M 2012 Calculations of two-fluid linear response to non-axisymmetric fields in tokamaks *Phys. Plasmas* **19** 056105
- [40] Reiser D and Chandra D 2009 Plasma currents induced by resonant magnetic field perturbations in tokamaks *Phys. Plasmas* **16** 042317
- [41] Kaveeva E and Rozhansky V 2012 Screening of resonant magnetic perturbations taking into account a self-consistent electric field *Nucl. Fusion* **52** 054011
- [42] Ferraro N M, Evans T E, Lao L L, Moyer R A, Nazikian R, Orlov D M, Shafer M W, Unterberg E A, Wade M R and Wingen A 2013 Role of plasma response in displacements of the tokamak edge due to applied non-axisymmetric fields *Nucl. Fusion* **53** 073042
- [43] Liu Y Q, Bondeson A, Fransson C M, Lennartson B and Breitholtz C 2000 Feedback stabilization of nonaxisymmetric resistive wall modes in tokamaks. I. electromagnetic model *Phys. Plasmas* **7** 3681–90
- [44] Liu Y Q *et al* 2016 Toroidal modelling of RMP response in ASDEX upgrade: coil phase scan, q(95) dependence, and toroidal torques *Nucl. Fusion* **56** 056015

- [45] Ferraro N M, Jardin S C and Snyder P B 2010 Ideal and resistive edge stability calculations with M3D-C1 *Phys. Plasmas* **17** 102508
- [46] Paz-Soldan C, Nazikian R, Cui L, Lyons B C, Orlov D M, Kirk A, Logan N C, Osborne T H, Suttrop W and Weisberg D B 2019 The effect of plasma shape and neutral beam mix on the rotation threshold for RMP-ELM suppression *Nucl. Fusion* **59** 056012
- [47] Nazikian R et al 2015 Pedestal bifurcation and resonant field penetration at the threshold of edge-localized mode suppression in the DIII-D tokamak *Phys. Rev. Lett.* **114** 105002
- [48] Suttrop W et al 2018 Experimental conditions to suppress edge localised modes by magnetic perturbations in the ASDEX upgrade tokamak *Nucl. Fusion* **58** 096031
- [49] Fitzpatrick R 2020 Theory of edge localized mode suppression by static resonant magnetic perturbations in the DIII-D tokamak *Phys. Plasmas* **27** 042506
- [50] Ryan D A et al 2015 Toroidal modelling of resonant magnetic perturbations response in ASDEX-upgrade: coupling between field pitch aligned response and kink amplification *Plasma Phys. Control. Fusion* **57** 095008
- [51] Zhang H W, Zhu J, Ma Z W, Kan G Y, Wang X and Zhang W 2019 Acceleration of three-dimensional Tokamak magnetohydrodynamical code with graphics processing unit and OpenACC heterogeneous parallel programming *Int. J. Comut. Fluid Dyn.* **33** 393–406
- [52] Zhang W, Ma Z W, Porcelli F, Zhang H W and Wang X 2020 Sawtooth relaxation oscillations, nonlinear helical flows and steady-state $m/n=1$ magnetic islands in low-viscosity tokamak plasma simulations *Nucl. Fusion* **60** 096013
- [53] Zhang W, Ma Z W, Lu X Q and Zhang H W 2020 Influence of shear flows on dynamic evolutions of double tearing modes *Nucl. Fusion* **60** 126022
- [54] Zhang W, Ma Z W and Wang S 2017 Hall effect on tearing mode instabilities in tokamak *Phys. Plasmas* **24** 102510
- [55] Garcia-Munoz M et al 2013 Fast-ion losses induced by ELMs and externally applied magnetic perturbations in the ASDEX upgrade tokamak *Plasma Phys. Control. Fusion* **55** 124014
- [56] Pustovitov V D 1998 Flux coordinates for tokamaks *Plasma Phys. Rep.* **24** 510–20
- [57] Zheng Z et al 2018 Kinetic equilibrium reconstruction for the NBI- and ICRH-heated H-mode plasma on EAST tokamak *Plasma Sci. Technol.* **20** 065103
- [58] Lao L et al 1985 Reconstruction of current profile parameters and plasma shapes in tokamaks *Nucl. Fusion* **25** 1611
- [59] Li Y Y et al 2014 Development of the charge exchange recombination spectroscopy and the beam emission spectroscopy on the EAST tokamak *Rev. Sci. Instrum.* **85** 11E428
- [60] Zhu J, Ma Z W, Wang S and Zhang W 2018 Nonlinear dynamics of toroidal Alfvén eigenmodes in the presence of tearing modes *Nucl. Fusion* **58** 046019
- [61] Zhang W, Ma Z W, Zhu J and Zhang H W 2019 Core-crash sawtooth associated with $m/n = 2/1$ double tearing mode in tokamak *Plasma Phys. Control. Fusion* **61** 075002
- [62] DeLucia J, Jardin S C and Todd A M M 1980 An iterative metric method for solving the inverse tokamak equilibrium problem *J. Comput. Phys.* **37** 183–204
- [63] Fu G Y and Van Dam J W 1989 Excitation of the toroidicity-induced shear Alfvén eigenmode by fusion alpha particles in an ignited tokamak *Phys. Fluids B* **1** 1949–52
- [64] Becoulet M et al 2008 Numerical study of the resonant magnetic perturbations for Type I edge localized modes control in ITER *Nucl. Fusion* **48** 024003